ChemPubSoc Europe

DOI: 10.1002/cssc.201903011

CHEMSUSCHEM Full Papers

In Operando Calorimetric Measurements for Activated Carbon Electrodes in Ionic Liquid Electrolytes under Large Potential Windows

Obaidallah Munteshari,[a, b] Arie Borenstein,[c, d] Ryan H. DeBlock,[e] Jonathan Lau,[e] Grace Whang,[e] Yucheng Zhou,[a] Ampol Likitchatchawankun,[a] Richard B. Kaner,[d, e, f] Bruce Dunn,[e, f] and Laurent Pilon*[a, f]

This study aims to investigate the effect of the potential window on heat generation in carbon-based electrical double layer capacitors (EDLCs) with ionic-liquid (IL)-based electrolytes using in operando calorimetry. The EDLCs consisted of two identical activated-carbon electrodes with either neat 1-butyl-1-methylpyrrolidinium bis(trifluoromethane-sulfonyl)imide ($[Pyr_{14}][TFSI]$) electrolyte or 1.0 M $[Pyr_{14}][TFSI]$ in propylene carbonate (PC) as electrolyte. The instantaneous heat generation rate at each electrode was measured under galvanostatic cycling for different potential windows ranging from 1 to 4 V. First, the heat generation rates at the positive and negative electrodes differed significantly in neat IL owing to the differences in the ion sizes and diffusion coefficients. However, these differences were minimized when the IL was diluted in PC. Second, for EDLC in neat $[Pyr_{14}][TFSI]$ at high potential window (4 V), a pronounced endothermic peak was observed at the beginning of the charging step at the positive electrode owing to $TFSI^-$ intercalation in the activated carbon. On the other hand, for EDLC in 1.0 M $[Pyr_{14}][TFSI]$ in PC at potential window above 3 V, an endothermic peak was observed only at the negative electrode owing to the decomposition of PC. Third, for both neat and diluted $[Pyr_{14}][TFSI]$ electrolytes, the irreversible heat generation rate increased with increasing potential window and exceeded Joule heating. This was attributed to the effect of potential-dependent charge redistribution resistance. A further increase in the irreversible heat generation rate was observed for the largest potential windows owing to the degradation of the PC solvent. Finally, for both types of electrolyte, the reversible heat generation rate increased with increasing potential window because of the increase in the amount of ion adsorbed/desorbed at the electrode/electrolyte interface.

Introduction

Electric double layer capacitors (EDLCs) have received significant attention in recent years for electrical energy storage applications, in particular those requiring high power and rapid charging, such as in regenerative braking of electric vehicles,[1] smart grids,[2] and renewable energy harvesting systems.[3–5] EDLCs consist typically of two carbon-based electrodes sandwiching a separator immersed in aqueous, organic, or ionic liquid (IL)-based electrolytes. EDLCs store electrical energy in the electrical double layer formed by ions at the electrode/electrolyte interface. They exhibit higher power density and longer cycle life than batteries but suffer from relatively low energy density E (in $J\,m^{-2}$). The latter can be expressed as,[4,6]

$$E = \frac{1}{2} C\,\Delta\psi_s^2 \tag{1}$$

where C is the specific capacitance of the cell (in $F\,m^{-2}$) and $\Delta\psi_s$ is the potential window (in V). One way to increase the energy density E consists of increasing the potential window $\Delta\psi_s$.[4] The latter, however, is usually limited by the chemical stability of the electrolyte.[7]

In recent years, ILs have been investigated as promising electrolytes in high-energy supercapacitors because of their

[a] Dr. O. Munteshari, Y. Zhou, A. Likitchatchawankun, Dr. L. Pilon
Mechanical and Aerospace Engineering Department
Henry Samueli School of Engineering and Applied Science
University of California
Los Angeles, CA 90095 (USA)
E-mail: pilon@seas.ucla.edu

[b] Dr. O. Munteshari
Mechanical Engineering Department
King Fahd University of Petroleum and Minerals (KFUPM)
Dhahran 31261 (Saudi Arabia)

[c] Dr. A. Borenstein
Chemistry Department
Ariel University, Ariel (Israel)

[d] Dr. A. Borenstein, Dr. R. B. Kaner
Chemistry and Biochemistry Department
University of California
Los Angeles, California 90095 (USA)

[e] R. H. DeBlock, Dr. J. Lau, G. Whang, Dr. R. B. Kaner, Dr. B. Dunn
Materials Science and Engineering Department
Henry Samueli School of Engineering and Applied Science
University of California
Los Angeles, CA 90095 (USA)

[f] Dr. R. B. Kaner, Dr. B. Dunn, Dr. L. Pilon
California NanoSystems Institute
University of California
Los Angeles, CA 90095 (USA)

Supporting Information and the ORCID identification number(s) for the author(s) of this article can be found under: https://doi.org/10.1002/cssc.201903011.

wide potential window and their operation at low temperatures.[7] However, ILs suffer from relatively high viscosity and low ionic conductivity compared with conventional aqueous and organic electrolytes resulting in large intrinsic resistance.[8,9] To overcome this limitation, diluting ILs in organic solvents have been proposed as a way to combine the favorable properties of ILs and organic electrolytes.[10–12] Another concern arising from the use of IL electrolytes is their stability under extreme potentials.[12,13] Despite ILs theoretically wide potential window, they may interact with high surface-area carbonaceous electrodes as a result of the catalytic activity of the electrode surface.[12,13] Thus, the electrochemical reactions of ILs at high potentials can significantly reduce the performance and lifetime of the cell or force the use of the narrower operating potential window and thus reduce the device energy density.[12,13] Understanding the stability of ILs under large potential windows can facilitate the optimization of IL-based supercapacitors.

Electrochemical experiments such as cyclic voltammetry and galvanostatic cycling are very informative methods to characterize oxidation and reduction reactions. However, to provide supplementary information and to gain insight into the nature of these reactions, complimentary in operando calorimetric measurements have been proposed.[14–16] Moreover, considering that EDLCs are designed to provide high current over a wide potential window and given the large cell resistance of IL-based electrolytes, it is essential to pay close attention to the heat generated for thermal management and safety purposes.

The present study aims to identify the thermal signatures of the different physicochemical phenomena taking place in EDLCs using neat IL electrolyte and IL diluted in organic solvent under galvanostatic cycling. To do so, the heat generation rate was measured for different potential windows using our newly developed in operando calorimeter.[14–16] Particular attention was paid to ion intercalation and electrolyte decomposition under large potential windows.

Background

The operating potential window is a key parameter for enhancing the specific energy of EDLCs. However, the operating potential window is limited by the electrochemical stability window of the electrolyte. Leyva-Garcia et al.[12] studied the electrochemical performance of porous activated carbon (AC) electrodes in (i) neat 1-butyl-1-methylpyrrolidinium bis(fluorosulfonyl)imide ([Pyr_{14}][TFSI]) and in (ii) 1.0 M [Pyr_{14}][TFSI] in PC electrolytes at different potential windows. For an AC negative electrode in 1.0 M [Pyr_{14}][TFSI] in PC electrolyte, a redox peak was observed in the CV curves for a half-cell potential window of $\simeq$1.3 V. In addition, the intensity of this redox peak increased with increasing potential window. However, no redox peak was observed in the CV curves obtained with identical electrodes but in neat [Pyr_{14}][TFSI] suggesting that the redox peak was owing to PC solvent decomposition.[12] In addition, Ruch et al.[17] have shown that the negative electrodes of symmetric EDLC in PC-based electrolytes degraded faster than the positive electrodes because of the presence of surface oxygen groups on the AC electrode that reacted with PC. Moreover, Hahn et al.[18] investigated the gas evolution during PC decomposition in EDLC using differential electrochemical mass spectrometry (DEMS). The authors found that, at a potential window of 2.7 V, PC reduced at the negative electrode to produce propane and hydrogen and oxidized at the positive electrode to release carbon dioxide.[18]

Similarly, Borenstein et al.[13] studied the failure mechanism of positive electrode in a symmetric EDLC under high cell potential. An EDLC cell consisting of AC electrodes and neat [Pyr_{14}][TFSI] was tested under galvanostatic cycling. The potential evolution was measured across each electrode of the EDLC during cycling by placing a silver pseudo-reference electrode sandwiched by two non-woven separators (NKK, Japan) between the two AC electrodes. Here, the potential window of the cell $\Delta\psi_s$ can be expressed as the difference between the potential evolution across the positive $\Delta\psi_+$ and negative $\Delta\psi_-$ ($\leq$0 V) half-cells (i.e., $\Delta\psi_s=\Delta\psi_+-\Delta\psi_-$). At low potential windows (i.e., $\Delta\psi_s\leq 3$ V), the potential evolution divided equally between the positive and negative electrodes $|\Delta\psi_+|=|\Delta\psi_-|$. However, for $\Delta\psi_s>3$ V, the potential evolution at the negative electrode was larger than that at the positive electrode (i.e., $|\Delta\psi_-|>|\Delta\psi_+|$). This asymmetry in the half-cell potentials was attributed to FSI^- intercalation into AC at the positive electrode, which increased its capacitance C_+. As the absolute amount of charge q at both electrodes must be identical, the potential at the negative electrode should increase according to,[4]

$$q = C_+\Delta\psi_+ = -C_-\Delta\psi_- \quad (2)$$

where C_+ and C_- are the capacitances of the positive and negative electrodes, respectively. This conclusion was further confirmed by scanning electron microscopy and energy dispersive X-ray spectroscopy (SEM-EDX) measurements indicating that a significant amount of FSI^- was present in the positive electrode after 3000 galvanostatic cycles for cell potential window $\Delta\psi=3.4$ V.[13]

Heat generation in EDLCs is a result of several interfacial, transport, and electrochemical processes.[19] It can be divided into irreversible and reversible heat generation rates.[14,15,19] The instantaneous irreversible heat generation rate $\dot{Q}_{irr}(t)$ in EDLCs under $\Delta\psi_s=1$ V has been reported to be mainly owing to Joule heating $\dot{Q}_J$ (in W) and expressed as,[14,15,19,20]

$$\dot{Q}_{irr}(t) = \dot{Q}_J(t) = R_s\, I(t)^2 \quad (3)$$

where R_s is the device internal resistance and I is the imposed current. However, Schiffer et al.[21] found that the temperature rise in EDLCs for $\Delta\psi_s=2$ V under galvanostatic cycling predicted by considering only Joule heating was smaller than that measured experimentally.[21] The analysis suggested that the irreversible heat generation rate in EDLCs was the summation of (i) Joule heating and (ii) heat generation owing to charge redistribution effects modeled as dissipation through the pore re-

sistance.[21–23] In fact, the charges redistribute themselves during cycling because of the non-uniform charging/discharging processes in the complex porous electrode structure.[22,23] Moreover, the measured temperature rise increased with increasing potential window suggesting that the pore resistance increased with increasing potential.[21]

The reversible heat generation in EDLCs can be attributed, in part, to the change in entropy of the electrolyte upon ion adsorption/desorption at the electrode surface.[19,21,24] When ions in the electrolyte adsorb on the electrode surface and form an EDL, the entropy decreases and consequently heat is generated.[14,19,21,24] This change in entropy is reversible over a full cycle resulting in exothermic charging and endothermic discharging.[14,19,21,24] Other physicochemical phenomena may also contribute to the irreversible and/or reversible heat generation rates. For example, in hybrid supercapacitors, redox reactions also contribute to the reversible heat generation upon charging/discharging.[16,25] In addition, the overpotential at the redox active electrode necessary to drive the redox reactions is responsible for irreversible "polarization heating".[16,25] Other possible sources of heat generation may be associated with ion solvation/desolvation and decomposition of the electrolyte at high potentials.[26]

Moreover, it is important to note that even if the electrodes of the cell are identical in composition and mass loading, the heat generation rate may be different at the positive and negative electrodes.[15,27] This difference can be attributed to differences in the valency, size, and/or diffusion coefficient of the anions and cations, as predicted numerically.[27] Indeed, d'Entremont and Pilon[27] developed a thermal model to estimate the spatiotemporal heat generation rate in EDLCs consisting of binary electrolytes with ion species with different valency, ion size, and/or diffusion coefficient. They observed that the ionic conductivity of the electrolyte increased with increasing ion valency and/or diffusion coefficient resulting in smaller irreversible heat generation rate at the respective electrode.[27] In addition, EDL formation by ions with smaller diameter and/or larger valency resulted in larger reversible heat generation rate during charging.[27] Differences in heat generation rates at each electrode can also be a result of interactions between ions and the electrode constituents, as observed experimentally for EDLCs.[14,15] Indeed, the reversible heat generation rate at the negative AC-based electrode containing carboxymethyl cellulose (CMC) as a binder and thickening agent was endothermic at the beginning of the charging step.[15] This was attributed to the overscreening effect resulting from the interactions between the anionic functional groups of CMC and Li^+ ions.[15]

In general, ILs consist of large organic cations coupled with smaller organic or inorganic anions with different diffusion coefficients.[7] For example, neat Pyr_{14}^+ and $TFSI^-$ (with a chemical formula of $[(CF_3SO_2)_2N]^-$) ions were estimated to have a diameter of $\approx$1.1 and $\approx$0.7 nm[28] with diffusion coefficients of $\approx 9.9\times10^{-12}$ and $\approx 8\times10^{-12}$ $m^2 s^{-1}$,[29] respectively. Adding an organic solvent to ILs can significantly influence the ion size and their transport properties owing to ion solvation.[30,31] For example, the ratio of the diffusion coefficients of Pyr_{14}^+ to $TFSI^-$ decreases from $\approx$1.23 in neat $[Pyr_{14}][TFSI]$ electrolyte to $\approx$1.05, when diluted in PC with molar ratio of 2:8.[29] In addition, $[Pyr_{14}][TFSI]$ also has a smaller ionic conductivity in its neat form than dissolved in PC, as previously discussed. Thus, one can expect different heat generation rates at the positive and negative electrodes when using neat or diluted IL electrolytes.

The present study aims to determine the irreversible and reversible heat generation rates associated with the physicochemical phenomena taking place at the positive and negative electrodes of EDLCs operating under extreme potential windows. The devices consisted of two identical activated carbon electrodes in neat $[Pyr_{14}][TFSI]$ electrolyte or in 1.0 M $[Pyr_{14}][TFSI]$ in PC electrolyte. In operando calorimetry can provide unique insights into phenomena occurring during charging/discharging and into the degradation mechanisms of the electrode and electrolyte in each half-cell.

Experimental Section

Electrode synthesis and device assembly

An activated carbon slurry was prepared by ball-milling (i) YP-50F AC (Kuraray), (ii) Super P (Alfa Aesar), and (iii) multiwall carbon nanotubes (mwCNT, Sigma Aldrich) as conducting additives with a weight ratio of 88:6:6. Then, the AC slurry was mixed with CMC (DOW Chemical) as a binder and thickening agent and styrene-butadiene rubber (SBR, MTI Corporation) binder with a weight ratio of 90:6:4. The slurry was then drop-cast onto 1×1 cm^2 current collectors made of 18 μm thick carbon-coated aluminum foil (MTI). The mass loading, for each electrode, was 2 mg cm^{-2} with a thickness of 40 ± 5 μm. The electrodes were dried under vacuum at 120 °C for 24 h before being placed in a glovebox under argon atmosphere. Two-electrode devices were assembled using a 1 mm thick chemically resistant polypropylene mesh acting as a separator and as a thermal insulator between the electrodes. The assembly was immersed in electrolyte consisting of either neat $[Pyr_{14}][TFSI]$ (Device 1) or 1.0 M $[Pyr_{14}][TFSI]$ in PC (Device 2). Finally, to avoid exposure to ambient atmosphere, the EDLCs were assembled, installed, and sealed in the isothermal calorimeter inside a glovebox. Table 1 summarizes the constituents of Devices 1 and 2 as well as the operating conditions considered. For both devices, the total mass loading was 4 mg cm^{-2} for the entire cell to facilitate comparison.

Table 1. Electrode compositions, electrolyte, and operating conditions for the two EDLCs investigated.

Device	Electrode	Mass loading [mg cm^{-2}]	Electrolyte	$\Delta\psi_s$ [V]	T [°C]
1	AC slurry	1.8	$[Pyr_{14}][TFSI]$	1–4	20
	SBR	0.12			
	CMC	0.08			
2	AC slurry	1.8	$[Pyr_{14}][TFSI]$ (1.0 M) in PC	1–3.5	20
	SBR	0.12			
	CMC	0.08			

In operando calorimeter

The time-dependent heat-generation-rate measurements were performed in Devices 1 and 2 using the in operando calorimeter apparatus described in Ref. [14]. In brief, the current collector of each electrode was in thermal contact with a thermoelectric heat flux sensor measuring the instantaneous heat generation rate therein.[14] The two electrodes were thermally insulated from one another by the 1 mm thick separator. The measurements were performed under isothermal conditions at a temperature of 20 °C.

The time-dependent heat generation rate $\dot{Q}_i(t)$ (in mW) at electrode "*i*" can be retrieved from the heat flux q''_i measured at the current collector/heat flux sensor interface according to,[14]

$$\dot{Q}_i(t) = q''_i \, A_i = \frac{\Delta V_i(t)}{S_i} A_i \tag{4}$$

where ΔV_i (*t*) is the voltage difference (in μV) measured across the thermoelectric heat flux sensor, S_i is the sensor sensitivity (in $\mu V\,cm^2\,mW^{-1}$), and A_i is the footprint area (in cm^2), respectively. Here, the sensor sensitivity S_i was provided by the manufacturer.[32] The subscript "*i*" refers to either the positive "+" or negative "−" electrode. The total instantaneous heat generation rate in the entire device can be determined by the summation of the instantaneous heat generation rates at the positive and negative electrodes of the cell [i.e., $\dot{Q}_T(t) = \dot{Q}_+(t) + \dot{Q}_-(t)$].

The time-dependent heat generation rate $\dot{Q}_i(t)$ at electrode "*i*" can be divided into irreversible $\dot{Q}_{irr,i}(t)$ and reversible $\dot{Q}_{rev,i}(t)$ heat generation rates [i.e., $\dot{Q}_i(t) = \dot{Q}_{irr,i}(t) + \dot{Q}_{rev,i}(t)$]. Unfortunately, $\dot{Q}_{irr,i}(t)$ is not always known unless it corresponds solely to Joule heating.[14,15,19,24] However, by definition, time-averaging the instantaneous reversible heat generation rate $\dot{Q}_{rev,i}(t)$ over an entire cycle yields $\bar{\dot{Q}}_{rev,i} = 0$. Thus, the time-averaged irreversible heat generation rate $\bar{\dot{Q}}_{irr,i}$ under galvanostatic cycling of period t_{cd} can be expressed as,

$$\bar{\dot{Q}}_{irr,i} = \frac{1}{t_{cd}} \int_{(n-1)t_{cd}}^{nt_{cd}} \dot{Q}_i(t)\, dt \text{ with } i = + \text{ or } - \tag{5}$$

where *n* is the cycle number taken sufficiently large to reach oscillatory steady state. The total time-averaged irreversible heat generation rate $\bar{\dot{Q}}_{irr,T}$ in the entire cell is expressed as $\bar{\dot{Q}}_{irr,T} = \bar{\dot{Q}}_{irr,+} + \bar{\dot{Q}}_{irr,-}$. To effectively compare the reversible heat generation rate at each electrode of the EDLCs, the time-averaged reversible heat generation rate $\bar{\dot{Q}}^{c}_{rev,i}$ during a galvanostatic charging step of duration t_c can be defined as (see Supporting Information),[14]

$$\bar{\dot{Q}}^{c}_{rev,i} = \frac{1}{t_c} \int_{(n-1)t_{cd}}^{(n-1)t_{cd}+t_c} \dot{Q}_i(t)\, dt - \bar{\dot{Q}}_{irr,i}. \tag{6}$$

Experimental procedure

First, the electrochemical stability window (ESW) of neat $[Pyr_{14}][TFSI]$ and 1.0 M $[Pyr_{14}][TFSI]$ in PC electrolytes was assessed using linear sweep voltammetry (LSV) at a slow scan rate of 0.1 $mV\,s^{-1}$. The LSV was performed on two freshly assembled two-electrode coin cells with AC electrodes synthesized as previously described. Positive and negative electrodes were separated by Whatman Glass Fiber D separator (Sigma–Aldrich) soaked in neat $[Pyr_{14}][TFSI]$ or 1.0 M $[Pyr_{14}][TFSI]$ in PC and tested using stainless steel coin cell parts (MTI). The coin cell was pressed to a pressure of ≈6 MPa inside of an argon-filled glovebox.

Second, cyclic voltammetry (CV) was performed on Devices 1 and 2 inside the calorimeter at scan rate ν ranging from 5 to 30 $mV\,s^{-1}$. The integral capacitance of the EDLCs was evaluated by integrating the area enclosed by the CV curve plotting the current *I*(*t*) vs. the imposed potential $\Delta\psi_s$ (*t*) for a given scan rate ν (in $mV\,s^{-1}$) and potential window between $\psi_{s,min}$ and $\psi_{s,max}$ as,[33]

$$C_{int}(\nu) = \frac{1}{\psi_{s,max} - \psi_{s,min}} \oint \frac{I}{2\nu} d\psi \tag{7}$$

Third, the time-dependent heat generation rate $\dot{Q}_i(t)$ at each electrode was measured under galvanostatic cycling with imposed constant current *I* ranging from 2 to 5 mA. The internal resistance R_s (or DC resistance, in Ω) of the device was determined from the IR drop observed at the charging/discharging transition of the cell potential $\Delta\psi_s$ (*t*) near t_c under galvanostatic cycling at a constant current *I* according to,[34–37]

$$R_s = \frac{\psi_s(t_c^+) - \psi_s(t_c^-)}{2I}. \tag{8}$$

Here, the IR drop $[\psi_s(t_c^+) - \psi_s(t_c^-)]$ was obtained by estimating the cell potential $\psi_s(t_c^-)$ 10 ms after the beginning of the discharging step at t_c^+ (i.e., $t_c^- - t_c^+ = 10$ ms), as suggested by Zhao et al.[35] Note that the cell potential window $\Delta\psi_s = \psi_{s,max} - \psi_{s,min}$ was varied from 1 V up to the maximum potential window before significant electrolyte degradation occurred, as determined by LSV. Here, the CV and heat generation rate measurements were successively performed for each potential window. Note also that the heat generation rate measurements at low current (i.e., $I \leq 1$ mA) fell below the detection level (< 10 μW) of the calorimeter and were ignored due to a low signal to noise ratio.

Results and Discussion

Electrochemical stability window

Figure 1 plots the LSVs for coin cells with AC electrodes with neat $[Pyr_{14}][TFSI]$ or 1.0 M $[Pyr_{14}][TFSI]$ in PC at room temperature and scan rate of 0.1 $mV\,s^{-1}$. Figure 1 indicates that the ESW for the neat $[Pyr_{14}][TFSI]$ was ≈4 V considering a threshold current of 50 μA, as suggested in Ref. [38]. In addition, the sharp increase in *I*(*t*) near $\psi_s \simeq 2.7$ V indicates that the PC-based $[Pyr_{14}][TFSI]$ decomposition started at ≈2.7 V instead of ≈4 V for neat $[Pyr_{14}][TFSI]$. This was because of the fact that PC decomposed at a potential window lower than that of neat $[Pyr_{14}][TFSI]$, as previously observed for a similar system.[12]

Cyclic voltammetry curves and capacitance

Figure 2 plots the measured CV curves for Device 1 at scan rates (a) $\nu = 5$ $mV\,s^{-1}$ and (b) $\nu = 30$ $mV\,s^{-1}$ with a potential window $\Delta\psi_s$ ranging from 1 to 4 V and for Device 2 at scan rates (c) $\nu = 5$ $mV\,s^{-1}$ and (d) $\nu = 30$ $mV\,s^{-1}$ with potential window $\Delta\psi_s$ ranging from 1 to 3.5 V. First, at a slow scan rate ($\nu = 5$ $mV\,s^{-1}$), the CV curves of both devices featured nearly rectangular and symmetrical shapes typical of the capacitive behavior of EDLCs. However, an increase in current was observed near $\psi_{s,max}$ for an increasing potential window. This increase in current was sharper in Device 2 than in Device 1 sug-

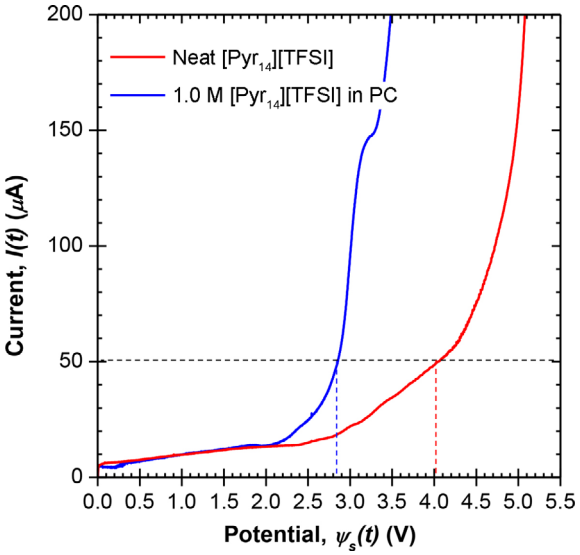

Figure 1. Linear sweep voltammograms for coin cells with neat [Pyr_{14}][TFSI] or 1.0 M [Pyr_{14}][TFSI] in PC at room temperature and scan rate of 0.1 mV s^{-1}.

gesting that it may be a result of PC solvent degradation, as previously observed for EDLCs using PC-based electrolytes.[12,23,39] Second, at a fast scan rate ($\nu = 30$ mV s^{-1}), the CV curves of Device 1 deviated from the near ideal capacitive behavior observed at slow scan rates. This resistive behavior was a result of the fact that neat [Pyr_{14}][TFSI] electrolyte suffers from low ionic conductivity and ion diffusion coefficient at room temperature.[28] On the other hand, CV curves of Device 2, using [Pyr_{14}][TFSI] diluted in PC, maintained their rectangular shape at fast scan rates. Indeed, the use of PC solvent reduced the viscosity of the electrolyte and increased the ion diffusion coefficient and ionic conductivity of the electrolyte, as summarized in Table 2. However, here also, Figure 2d indicates that the CV curve of Device 2 at $\nu = 30$ mV s^{-1} and $\Delta\psi_s =$ 3.5 V featured a rise in current near $\psi_{s,\,max}$ owing to PC degradation.

Table 2. Transport properties of neat [Pyr_{14}][TFSI] and 1.0 M [Pyr_{14}][TFSI] in PC electrolytes.

Property	Electrolyte [Pyr_{14}][TFSI]		Ref.
	neat	1.0 M in PC	
ionic conductivity [mS cm^{-1}]	2.6	10.3	[9]
viscosity [MPa s]	62	5.6	[9]
Pyr_{14}^{+} diameter [nm]	≈1.1	–	[28]
$TFSI^{-}$ diameter [nm]	≈0.7	–	[28]
Pyr_{14}^{+} diffusion coefficient [m^2 s^{-1}]	$\approx 9.9\times10^{-12}$	$\approx 1.8\times10^{-10}$	[29]
$TFSI^{-}$ diffusion coefficient [m^2 s^{-1}]	$\approx 8.0\times10^{-12}$	$\approx 1.7\times10^{-10}$	[29]

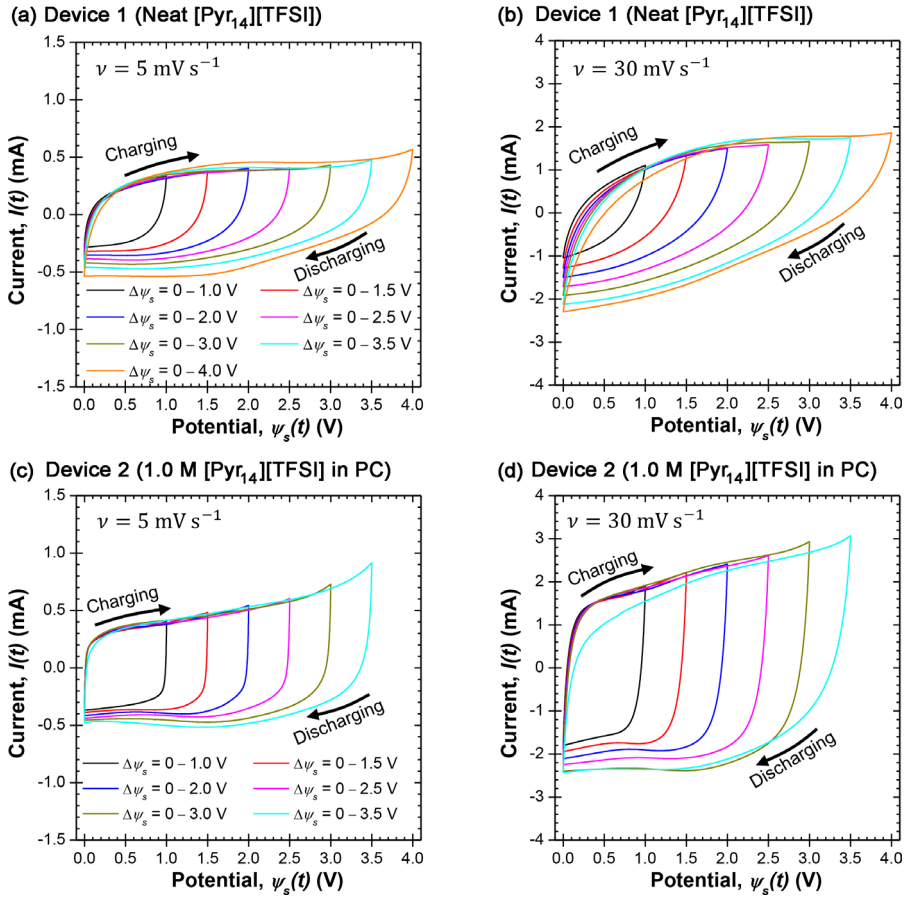

Figure 2. CV curves for Device 1 at scan rates (a) $\nu = 5$ mV s^{-1} and (b) $\nu = 30$ mV s^{-1} with potential window $\Delta\psi_s$ ranging from 1 to 4 V and for Device 2 at scan rates (c) $\nu = 5$ mV s^{-1} and (d) $\nu = 30$ mV s^{-1} with potential window $\Delta\psi_s$ ranging from 1 to 3.5 V.

Figure 3 shows the integral capacitance $C_{int}(\nu)$ of (a) Device 1 and (b) Device 2 as a function of scan rate ν ranging from 5 to 30 mV s^{-1} for different potential windows. For both devices,

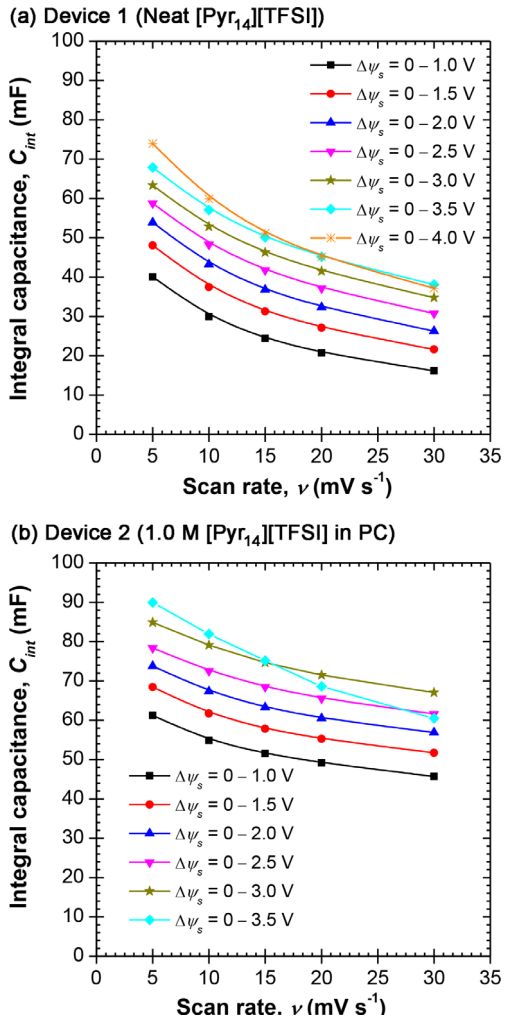

Figure 3. Integral capacitance $C_{int}(\nu)$ of (a) Device 1 and (b) Device 2 as a function of scan rate ν calculated [Eq. (7)] from their corresponding CV curves (Figure 2) for different potential windows $\Delta\psi_s$.

$C_{int}(\nu)$ decreased with increasing scan rate, as typically observed in various electrochemical capacitors.[40,41] Note that, for any given scan rate ν and potential window $\Delta\psi_s$, Device 2 featured integral capacitance larger than that of Device 1. This confirms that diluting IL in PC enhances the transport properties and dielectric constant of the electrolyte, thus improving the capacitance of the EDLC at room temperature.[42] In addition, $C_{int}(\nu)$ generally increased with increasing potential window except for $\Delta\psi_s = 4$ V for Devices 1 and $\Delta\psi_s = 3.5$ V for Device 2. For these potential windows, $C_{int}(\nu)$ of both devices decreased faster with increasing scan rate compared with smaller potential windows. This can be attributed to the fact that the electrolytes of both devices degraded at large potential windows. However, Figure 3 alone does not indicate if both electrodes degraded equally or if one was more affected by the large potential window than the other.

Galvanostatic cycling and internal resistance

Figure 4 shows the temporal evolution of the cell potential $\psi_s(t)$ during galvanostatic cycling for Device 1 at current (a) $I =$ 2 mA and (b) $I = 5$ mA and for Device 2 at current (c) $I = 2$ mA and (d) $I = 5$ mA and for potential window $\Delta\psi_s$ varying from 1 to 4 V. Figure 4 indicates that, for both devices, $\psi_s(t)$ varied almost linearly with time between $\psi_{s,\,min}$ and $\psi_{s,\,max}$, except at the transitions between the charging and discharging steps owing to the IR drop. The latter was larger in Device 1 than in Device 2. It is interesting to note that the temporal evolution of $\psi_s(t)$ overlapped for the different potential windows $\Delta\psi_s$(i) less than 3.5 V for Device 1 and (ii) less than 3 V for Device 2. However, in both devices, for the largest potential windows considered, the potential $\psi_s(t)$ rose faster during charging corresponding to a decrease in the capacitance observed in the CV measurements at these potential windows. In addition, the IR drop was independent of the potential window except at the largest potential window. This resistive behavior observed at large potential windows can be attributed to electrolyte degradation in both devices. Finally, for Device 1 at $I = 5$ mA and $\Delta\psi_s \leq 2$ V, the cycle period t_{cd} was less than 5 s because of the large IR drop and the small capacitance. Then, the charging time was not significantly larger than the response time of the calorimeter of 0.7 s.[14] Thus, the heat generation rate measurements for Device 1 at $\Delta\psi_s \leq 2$ V were only reported for current I ranging from 2 to 4 mA.

Figure 5 plots the internal resistance R_s as a function of imposed current I ranging from 2 to 5 mA estimated from Equation (8) for (a) Device 1 and (b) Device 2. For both devices, the internal resistance R_s was nearly independent of the imposed current I for all potential windows considered. It was also independent of potential window for (i) $\Delta\psi_s \leq 3.5$ V for Device 1 and (ii) $\Delta\psi_s \leq 3$ V for Device 2. For these potential windows, the internal resistance of Device 1 ($81.6 \pm 9\ \Omega$) was more than three times that of Device 2 ($23.7 \pm 5\ \Omega$). Again, this was due to the fact that the ionic conductivity of 1.0 M of [Pyr$_{14}$][TFSI] in PC was nearly three times larger than that of neat [Pyr$_{14}$][TFSI] (Table 2). However, for potential windows beyond 3.5 V for Device 1 and 3 V for Device 2, R_s increased significantly. In fact, the resistance of Device 1 increased from 81.6 ± 9 to $102.5 \pm 6\ \Omega$, whereas that of Device 2 increased from 23.7 ± 5 to $46.6 \pm 5\ \Omega$. This can be attributed to electrolyte degradation of both devices at a large potential window, as discussed earlier.

Instantaneous heat generation rates

Figure 6 shows the temporal evolution of the measured heat generation rates $\dot{Q}_+(t)$ at the positive electrode, $\dot{Q}_-(t)$ at the negative electrode, and $\dot{Q}_T(t)$ in the entire cell for Device 1 for potential windows of (a) $\Delta\psi_s = 2$, (b) 2.5 V, (c) 3 V, (d) 3.5 V, and (e) 4 V as functions of the dimensionless time t/t_{cd} for five representative and consecutive galvanostatic cycles at a constant current $I = 4$ mA. Similarly, Figure 7 plots the heat generation rates $\dot{Q}_+(t)$, $\dot{Q}_-(t)$, and $\dot{Q}_T(t)$ for Device 2 for potential windows of (a) $\Delta\psi_s = 1$ V, (b) 1.5 V, (c) 2 V, (d) 2.5 V, (e) 3 V, and

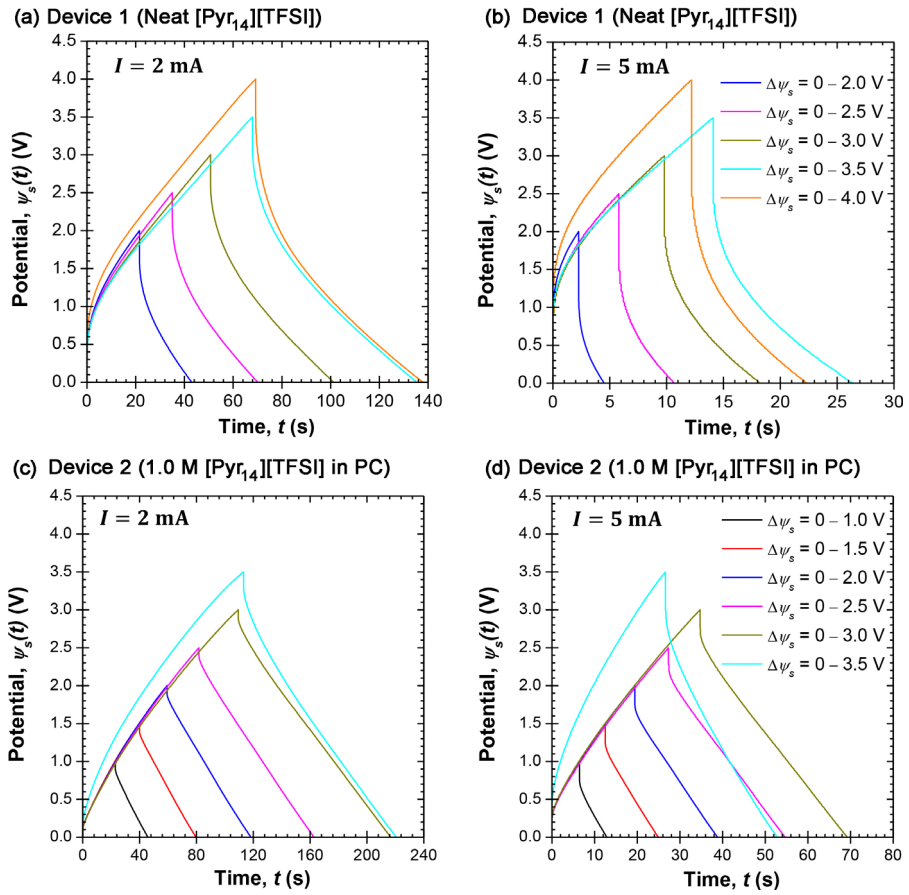

Figure 4. Galvanostatic charging/discharging curves for Device 1 at current (a) $I=2$ mA and (b) $I=5$ mA and for Device 2 at current (c) $I=2$ mA and (d) $I=5$ mA for different potential windows between 1 and 4 V.

(f) 3.5 V as functions of the dimensionless time t/t_{cd} for five representative and consecutive galvanostatic cycles at a constant current $I=4$ mA. First, for both devices, measurements of the instantaneous heat generation rates at the positive and negative electrodes were repeatable cycle after cycle. In addition, in both devices, the magnitude of $\dot{Q}_{+}(t)$, $\dot{Q}_{-}(t)$, and $\dot{Q}_{T}(t)$ increased with increasing potential window $\Delta\psi_s$. However, for any given current I and potential window $\Delta\psi_s$, the heat generation rate in Device 1 was larger than that in Device 2 because of the larger electrical resistance of the neat IL (Figure 5). It is also interesting to note that, in Device 1, the magnitude and shape of $\dot{Q}_{+}(t)$ at the positive electrode were larger and different from that of $\dot{Q}_{-}(t)$ at the negative electrode. However, $\dot{Q}_{+}(t)$ and $\dot{Q}_{-}(t)$ were nearly identical in Device 2 except for $\Delta\psi_s \geq 3$ V. These observations will be explained later.

Moreover, the heat generation rate $\dot{Q}_{-}(t)$ at the negative electrode of either device featured an endothermic dip observed previously at the beginning of the charging step. This dip was attributed to the overscreening effect with $LiPF_6$ in ethylene carbonate dimethyl carbonate (EC:DMC) in the presence of CMC binder.[15] However, this drop in $\dot{Q}_{-}(t)$ was not as large compared with our previous observations reported in Ref. [15], especially at low potential windows. This could be attributed to the fact that the size of the ions Pyr_{14}^{+} ($\approx$1.1 nm)[28] used in this study is much larger than that of solvated Li^{+} ($\approx$0.41 nm)[43] used in Ref. [15]. Thus, the relatively large Pyr_{14}^{+} ions could not easily insert and could be trapped in the sub-nanoscale pores of the negative electrodes, and would minimize the overscreening effect.

$TFSI^{-}$ ion intercalation

For Device 1, $\dot{Q}_{+}(t)$ and $\dot{Q}_{-}(t)$ featured an endothermic dip at the beginning of the charging step whose magnitude increased with increasing potential window starting at $\Delta\psi_s=$ 3.5 V (Figure 6e). This peak was more prominent at the positive electrode at $\Delta\psi_s=4$ V and could be attributed to intercalation of $TFSI^{-}$ ions into nano-graphite clusters that generally exist in amorphous carbon-based electrodes.[13] Indeed, the intercalation of $TFSI^{-}$ into graphite positive electrodes has been reported in several studies.[44–47] To confirm this hypothesis, energy dispersive X-ray spectroscopy (EDX) measurements were performed on the positive and negative electrodes of two identical coin cells in neat $[Pyr_{14}][TFSI]$ electrolyte fabricated, as previously described for LSV measurements. Prior to EDX measurements, the two coin cells were cycled under galvanostatic conditions at current $I=4$ mA for 1000 cycles each at different potential windows namely $\Delta\psi_s=1$ V and $\Delta\psi_s=4$ V.

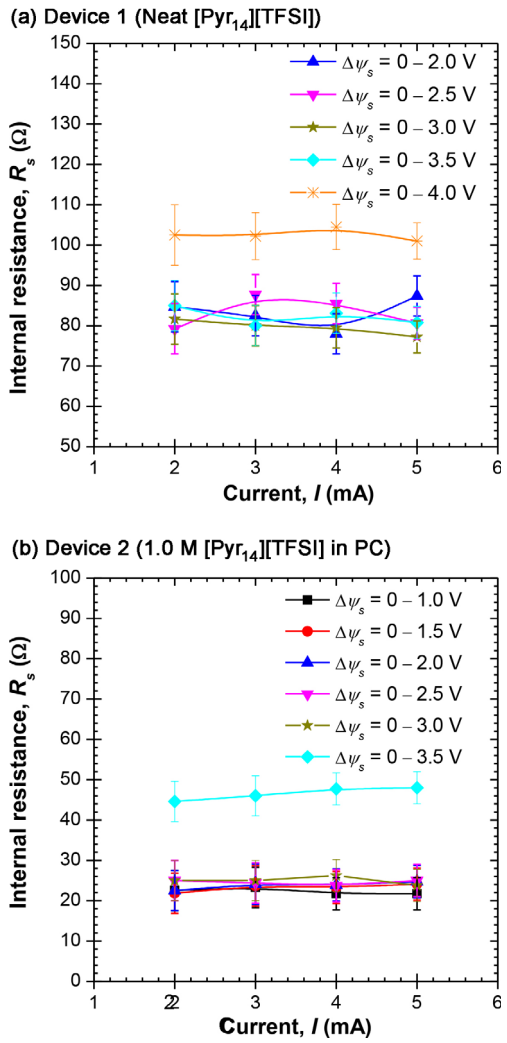

Figure 5. Internal resistance R_s of (a) Device 1 and (b) Device 2 estimated from IR drop [Eq. (8)] as a function of imposed current I ranging from 2 to 5 mA for potential window $\Delta\psi_s$ varying from 1 to 4 V.

Then, the electrodes were washed thoroughly with PC and dried. Figure 8 shows the EDX measurements for (a) the positive and (b) negative electrodes of the first coin cell using neat [Pyr_{14}][TFSI] after 1000 cycles at a constant current $I=4$ mA and $\Delta\psi_s=1$ V and for (c) the positive and (d) negative electrodes of the second coin cell after 1000 cycles at a constant current $I=4$ mA, but $\Delta\psi_s=4$ V. Figure 8(c) indicates that a significant amount of sulfur and fluorine were found in the positive electrode of the coin cell cycled at $\Delta\psi_s=4$ V compared not only to the negative counter electrode, but also to the positive electrode of the other coin cell cycled at $\Delta\psi_s=1$ V. These results establish that $TFSI^-$ intercalated into the positive electrode at sufficiently high potentials. Thus, the heat generation associated with non-spontaneous ion intercalation was endothermic, as observed for similar intercalation processes.[16]

PC degradation

For Device 2, only $\dot{Q}_-(t)$ at the negative electrode featured an endothermic dip at the beginning of the charging step for large potential windows. This peak appeared first at $\Delta\psi_s=3$ V (Figure 7e) and became stronger at $\Delta\psi_s=3.5$ V (Figure 7f). These observations can be attributed to the fact that the PC solvent decomposed at potentials exceeding 3 V (Figure 1). In addition, the PC decomposition occurred first at the negative electrode, as observed previously in similar systems with PC-based electrolytes.[12,17] Here, the PC reduction at the negative electrode started at $\Delta\psi_s=3$ V. Moreover, the PC reduction was an endothermic process. However, it only dominated at the beginning of the charging step due to the competing exothermic heat generation occurring owing to ion adsorption and possible desolvation.

Irreversible heat generation rates

Figure 9 plots the time-averaged irreversible heat generation rates $\bar{\dot{Q}}_{irr,+}$ at the positive electrode and $\bar{\dot{Q}}_{irr,-}$ at the negative electrode for (a) Device 1 and (b) Device 2 as functions of potential window $\Delta\psi_s$ for current I ranging between 2 and 5 mA. The error bars correspond to two standard deviations or 95% confidence interval estimated by evaluating $\bar{\dot{Q}}_{irr,i}$ over five consecutive galvanostatic cycles. Figure 9a indicates that $\bar{\dot{Q}}_{irr,+}$ was larger than $\bar{\dot{Q}}_{irr,-}$ in Device 1 for all currents and potential windows considered. This can be attributed to the fact that the resistance of the positive half-cell was larger than that of the negative half-cell. Indeed, the ionic conductivity of the electrolyte is linearly proportional to the diffusion coefficient[48] and the diffusion coefficient of $TFSI^-$ is smaller than that of Pyr_{14}^+ in neat [Pyr_{14}][TFSI] ionic liquid (Table 2). By contrast, Figure 9b establishes that $\bar{\dot{Q}}_{irr,+}$ and $\bar{\dot{Q}}_{irr,-}$ were nearly the same in Device 2. This can be attributed to the fact that the diffusion coefficients of Pyr_{14}^+ and $TFSI^-$ were also nearly identical when diluted in PC solvent.[29,49] The slight difference could be attributed to differences in the electrode mass loading and/or capacitance.

Figure 9 also plots the total time-averaged irreversible heat generation rate $\bar{\dot{Q}}_{irr,T}$ for (c) Device 1 and (d) Device 2 under galvanostatic cycling as a function of potential window $\Delta\psi_s$ for current I ranging between 2 and 5 mA. First, for both devices, $\bar{\dot{Q}}_{irr,T}$ increased not only with increasing current I but also with increasing potential window ψ_s. However, it has been established experimentally for carbon-based EDLCs with low potential windows ($\Delta\psi_s \leq 1$ V),[14,15,20,21,24] that Joule heating was the dominant source of irreversible heat generation. In addition, the internal resistance R_s was found to be independent of potential window (Figure 5). Thus, the heat generation rate owing to Joule heating and given by $\bar{\dot{Q}}_J = R_s I^2$ should be independent of potential window for a given current I. However, such predictions were not observed in Figure 9. Therefore, there is an additional source of irreversible heat generation contributed to $\dot{Q}_{irr}(t)$ in addition to Joule heating. This contribution increased with increasing potential window. This could be attributed to the heat generation associated with charge redistribution effects in the porous carbon electrode and modeled as the leakage current dissipated through the pore resistance.[21] Indeed, the pore resistance is responsible for self-discharge (leakage current) in EDLCs along with other parasitic re-

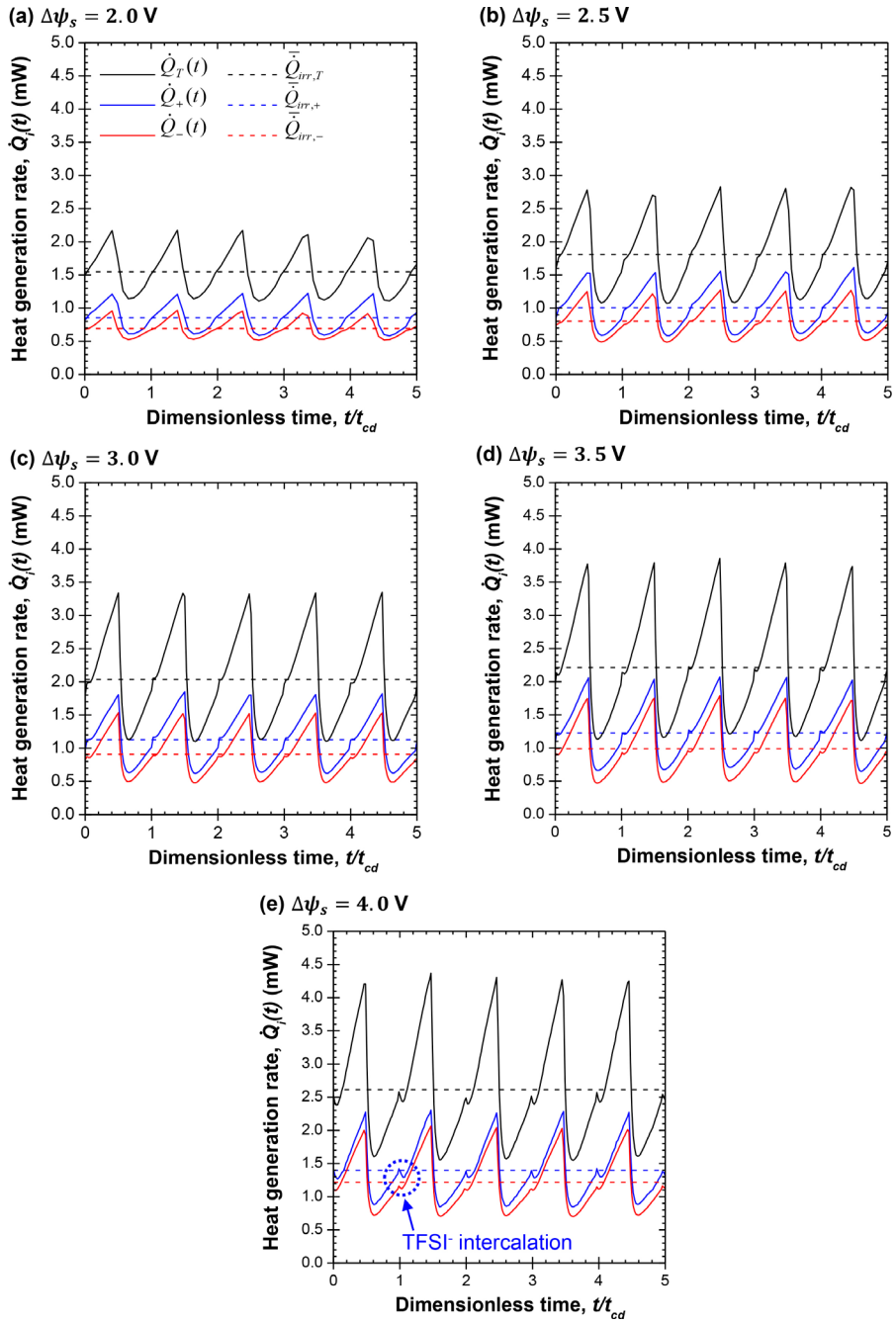

Figure 6. Heat generation rates $\dot{Q}_+(t)$ at the positive electrode, $\dot{Q}_-(t)$ at the negative electrode, and $\dot{Q}_T(t)$ in the entire cell for Device 1 for potential window (a) $\Delta\psi_s = 2$ V, (b) 2.5 V, (c) 3 V, (d) 3.5 V, and (e) 4 V as functions of the dimensionless time t/t_{cd} for five representative and consecutive galvanostatic cycles at a constant current $I = 4$ mA.

actions, such as electrolyte decomposition, and oxidation/reduction of carbon surface functional groups.[22,50] In addition, this contribution increased with increasing potential window as the pore resistance also increased with increasing potential window.[21] This response can be attributed to the fact that, with increasing the potential window, (i) more ions accumulate at the electrode/electrolyte interface and (ii) the time of charging/discharging is longer allowing more charge redistribution to take place. This, in turn, caused the sharp increase in heat generation rate at the end of each charging step (Figures 6 and 7). Finally, the additional contribution to the heat generation rate was more significant at small currents (see Supporting Information). This can be attributed to the fact that, at smaller currents, the charging/discharging time was longer allowing more charge redistribution to take place. This, in turn, led to more heat dissipation.

Reversible heat generation rates

The previous discussion indicates that the instantaneous irreversible heat generation rate $\dot{Q}_{irr,i}(t)$ cannot be estimated as solely Joule heating because of the additional contribution

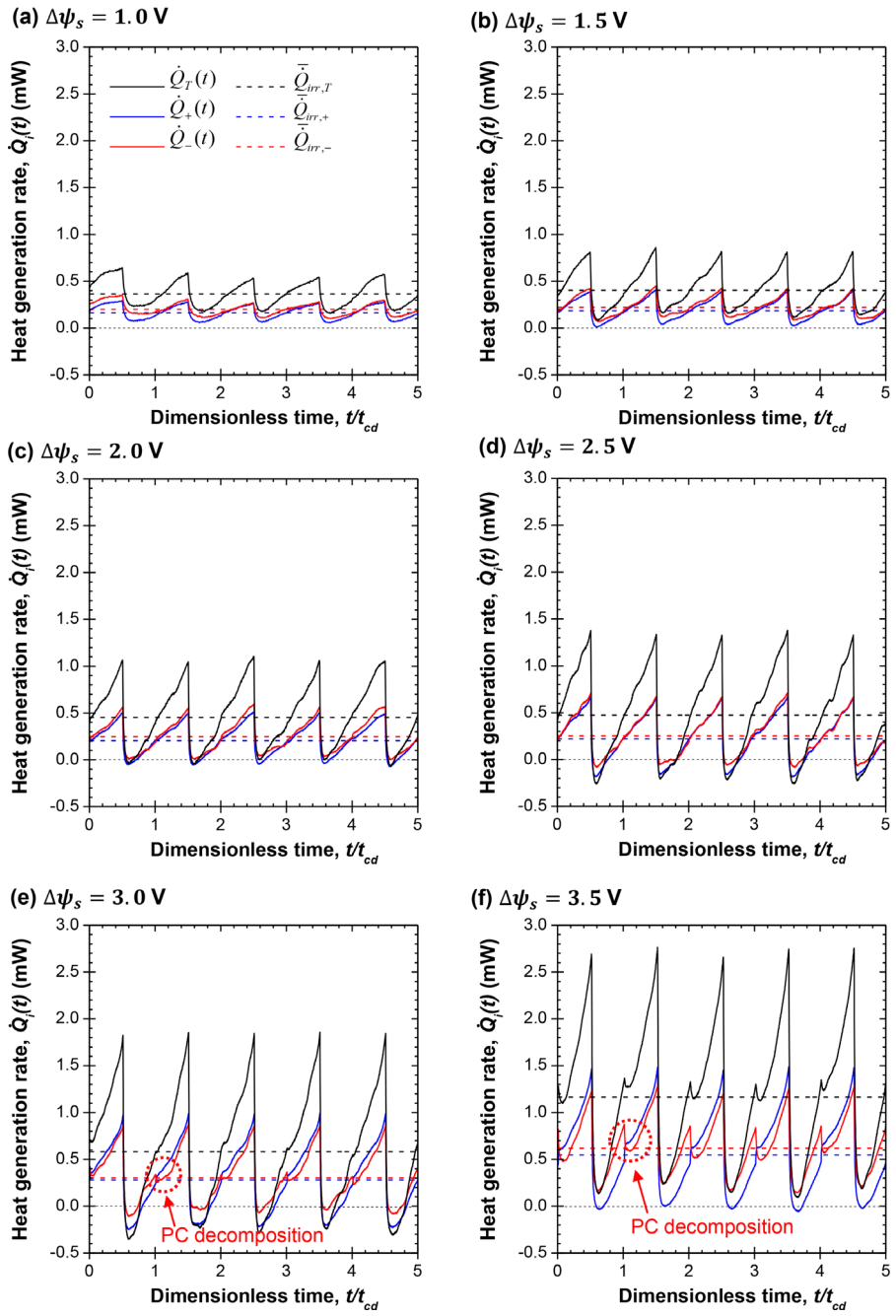

Figure 7. Heat generation rates $\dot{Q}_+(t)$ at the positive electrode, $\dot{Q}_-(t)$ at the negative electrode, and $\dot{Q}_T(t)$ in the entire cell for Device 2 for potential window (a) $\Delta\psi_s = 1$ V, (b) 1.5 V, (c) 2 V, (d) 2.5 V, (e) 3 V, and (f) 3.5 V as functions of the dimensionless time t/t_{cd} for five representative and consecutive galvanostatic cycles at a constant current $I = 4$ mA.

from charge redistribution. Therefore, the instantaneous reversible heat generation rate $\dot{Q}_{rev,i}(t) = \dot{Q}_i(t) - \dot{Q}_{irr,i}(t)$ cannot be measured either. Instead, the time-averaged reversible heat generation rate during charging $\bar{\dot{Q}}^c_{rev,i}$ was computed based on Equation (6).

Figure 10 plots $\bar{\dot{Q}}^c_{rev,+}$ at the positive electrode and $\bar{\dot{Q}}^c_{rev,-}$ at the negative electrode for (a) Device 1 and (b) Device 2 as functions of potential window $\Delta\psi_s$ for currents $I = 2$ mA and 5 mA. Results for other currents are available in the Supporting Information. Here also, the reported values of $\bar{\dot{Q}}^c_{rev,i}$ were averaged over five consecutive cycles and the error bars correspond to the 95% confidence interval. First, Figure 10a indicates that $\bar{\dot{Q}}^c_{rev,+}$ was larger than $\bar{\dot{Q}}^c_{rev,-}$ in Device 1. This can be attributed to the fact that the size of Pyr^+_{14} ions (≈1.1 nm) is larger than that of $TFSI^-$ (≈0.7 nm) in neat IL.[28] Indeed, previous numerical simulations have established that the reversible heat generation decreased with increasing counter ion diameter.[27] Here, the larger Pyr^+_{14} ions were adsorbed at the negative electrode causing less reversible heat generation than the smaller $TFSI^-$ ion adsorption at the positive electrode. Howev-

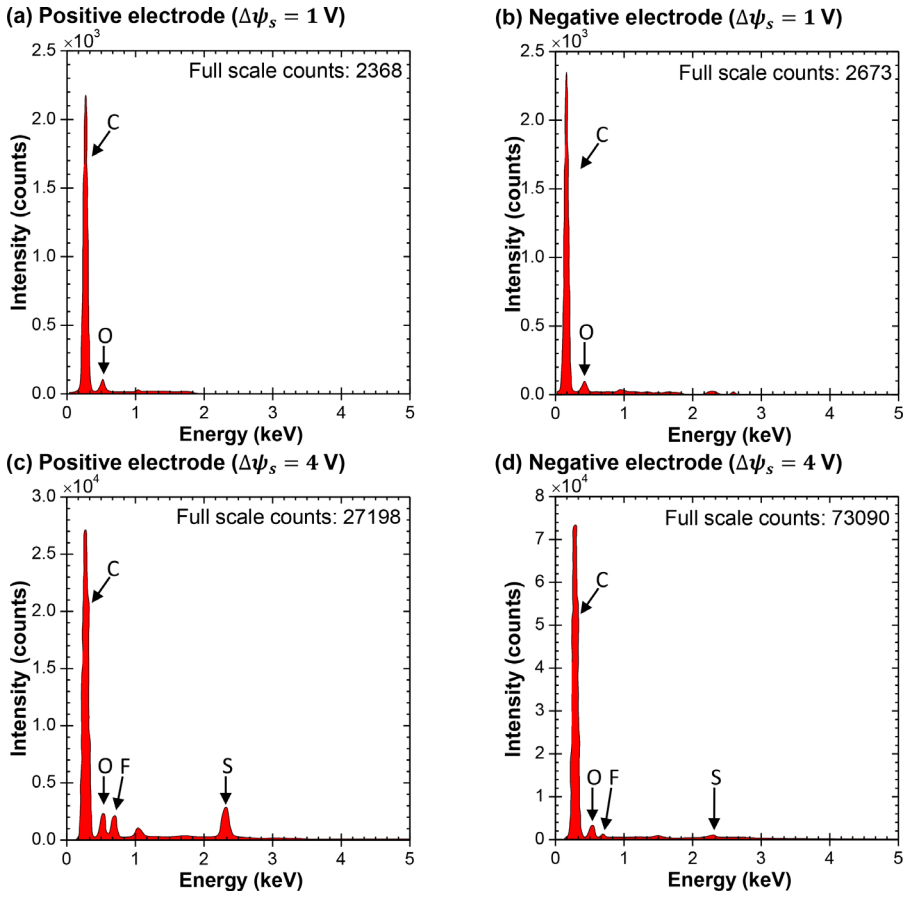

Figure 8. EDX measurements of (a, c) the positive and (b, d) negative electrodes of AC-based coin cells using neat [Pyr_{14}][TFSI] after 1000 constant current cycles at $I = 4$ mA with potential window of (a, b) $\Delta\psi_s = 1$ V and (c, d) $\Delta\psi_s = 4$ V, respectively.

er, when [Pyr_{14}][TFSI] was diluted in PC (Device 2), $\bar{Q}^c_{rev,+}$ and $\bar{Q}^c_{rev,-}$ [Figure 10b] were nearly identical for potential windows $\Delta\psi_s \leq 2.5$ V. These observations were a result of the fact that Pyr^+_{14} and $TFSI^-$ get solvated in PC resulting in similar diffusion coefficients (Table 2) and therefore similar effective ion size, as suggested by the Stokes–Einstein model.[51] Figure 10a also indicates that both $\bar{Q}^c_{rev,+}$ and $\bar{Q}^c_{rev,-}$ in Device 1 increased with increasing potential window for any given current I except at $\Delta\psi_s \simeq 3.5$ V when $\bar{Q}^c_{rev,+}$ started decreasing because of partially reversible endothermic intercalation of $TFSI^-$ into AC at the positive electrode, as discussed earlier. Similarly, Figure 10b shows that $\bar{Q}^c_{rev,-}$ in Device 2 decreased at large potential windows ($\Delta\psi_s \geq 3$ V) owing to the endothermic PC solvent decomposition previously observed in Figures 7e, f and in similar systems.[12,17]

Finally, Figure 10 plots the total time-averaged reversible heat generation rate normalized by the current I (i.e., $\bar{Q}^c_{rev,T}/I$) for (c) Device 1 and (d) Device 2 under galvanostatic cycling as a function of potential window $\Delta\psi_s$ for currents I ranging from 2 to 5 mA. First, Figures 10c, d indicate that, for both devices, $\bar{Q}^c_{rev,T}/I$ curves nearly overlap indicating that the time-averaged reversible heat generation rate during the charging step $\bar{Q}^c_{rev,T}$ in the entire cell was positive and linearly proportional to the imposed current I. This result was consistent with previous experimental observations[14,15,20,21,24] and numerical predictions[19] for EDLCs. It is also interesting to note that, for both devices, $\bar{Q}^c_{rev,T}/I$ increased with increasing potential window $\Delta\psi_s$. This can be attributed to the fact that increasing the potential window increased the amount of ions accumulated in the EDL forming at the electrode/electrolyte interface and thus the associated change in entropy of the electrolyte responsible for reversible heat generation.[19,21]

Conclusions

In operando calorimetry was used to investigate the heat generation rate in electrical double layer capacitors (EDLCs) with ionic liquid (IL)-based electrolytes under galvanostatic cycling for different potential windows. The EDLCs consisted of two identical activated carbon electrodes with either neat 1-butyl-1-methylpyrrolidinium bis(trifluoromethane-sulfonyl)imide ([Pyr_{14}][TFSI]) electrolyte or 1.0 M [Pyr_{14}][TFSI] in propylene carbonate (PC) electrolytes. First, the instantaneous heat generation rate at the positive and negative electrodes in both devices increased with increasing potential window. Second, the heat generation rate at the positive electrode in neat IL was significantly different from that at the negative electrode owing to differences in ion sizes and diffusion coefficients. In-

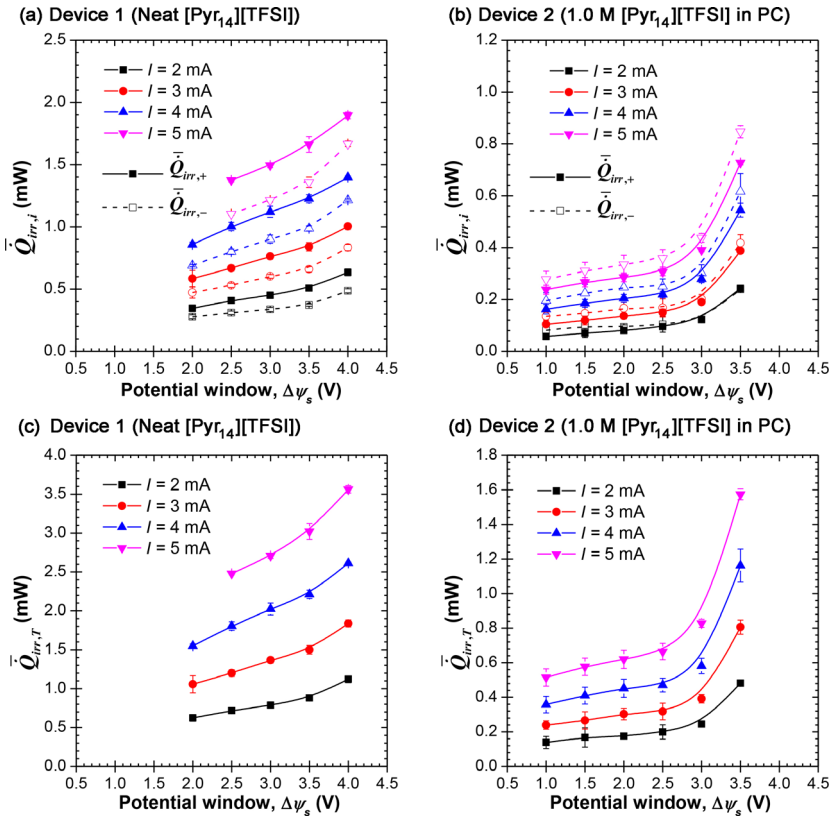

Figure 9. Time-averaged irreversible heat generation rate $\bar{Q}_{irr,+}$ at the positive electrode and $\bar{Q}_{irr,-}$ at the negative electrode for (a) Device 1 and (b) Device 2 as functions of potential window $\Delta\psi_s$. Total time-averaged irreversible heat generation rate $\bar{Q}_{irr,T}$ for (c) Device 1 and (d) Device 2 under galvanostatic cycling as a function of potential window $\Delta\psi_s$ for current I ranging between 2 and 5 mA.

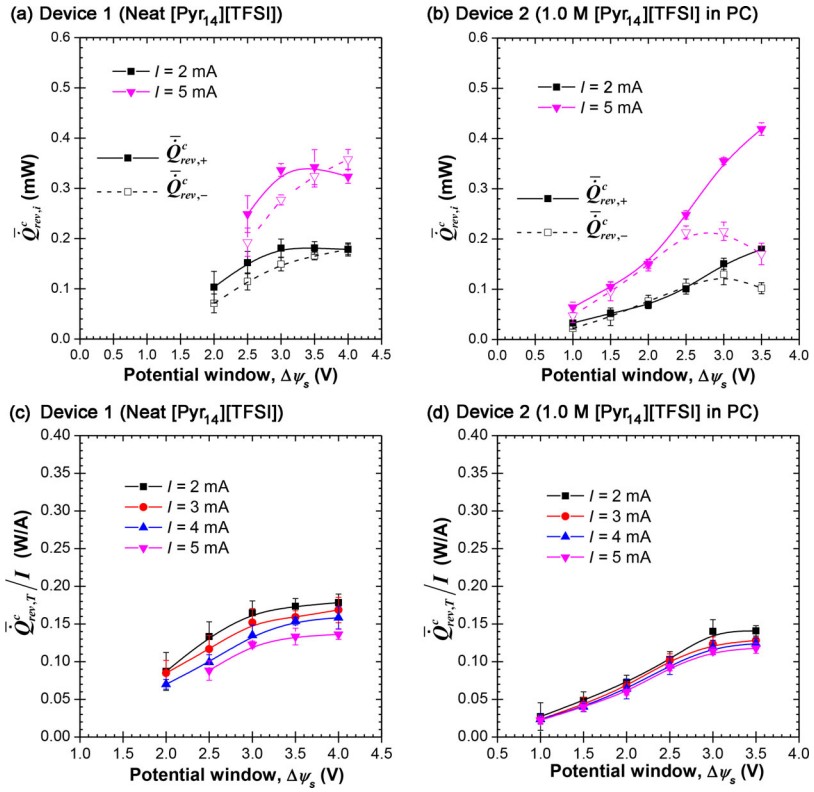

Figure 10. Time-averaged reversible heat generation rate $\bar{Q}^c_{rev,+}$ at the positive electrode and $\bar{Q}^c_{rev,-}$ at the negative electrode for (a) Device 1 and (b) Device 2 as functions of potential window $\Delta\psi_s$. Total time-averaged reversible heat generation rate normalized by current, i.e., $\bar{Q}^c_{rev,T}/I$ for (c) Device 1 and (d) Device 2 under galvanostatic cycling as a function of potential window $\Delta\psi_s$ for current I ranging between 2 and 5 mA.

terestingly, such differences were not observed when the IL was dissolved in PC because of ion solvation. Third, for EDLC in neat $[Pyr_{14}][TFSI]$ at a high potential window (4 V), an endothermic dip was observed in both electrodes at the beginning of the charging step owing to the electrolyte decomposition. However, it was more pronounced at the positive electrode because of $TFSI^-$ intercalation. On the other hand, for EDLC in 1.0 M $[Pyr_{14}][TFSI]$ in PC at a high potential window ($\geq$3 V), an endothermic dip was only observed at the negative electrode because of PC decomposition. Fourth, as the potential window increased, the irreversible heat generation rate exceeded Joule heating. This was attributed to heat dissipation owing to charge redistribution resistance in the porous electrodes. A further increase in the irreversible heat generation was observed at a very high potential window owing to electrolyte degradation. Finally, the time-averaged reversible heat generation rate was nearly proportional with current, but increased with increasing potential window because of the increase in the amount of ion adsorbed/desorbed during electrical double layer formation/dispersion at the electrode/electrolyte interface.

Acknowledgements

This work was supported as part of the Center for Synthetic Control Across Length-scales for Advancing Rechargeables (SCALAR), an Energy Frontier Research Center funded by the U.S. Department of Energy, Office of Science, Basic Energy Sciencesunder Award # DE-SC0019381. O.M. is grateful for the financial support provided by King Fahd University of Petroleum and Minerals (KFUPM), Dhahran, Saudi Arabia. R.B.K. thanks the Dr. Myung Ki Hong Endowed Chair in Materials Innovation.

Conflict of interest

The authors declare no conflict of interest.

Keywords: activated carbon · electrolyte degradation · ionic liquids · thermal management · thermal runaway

[1] L. Zhang, Z. Wang, X. Hu, F. Sun, D. G. Dorrell, *J. Power Sources* **2015**, *274*, 899 – 906.
[2] S. Koohi-Kamali, V. V. Tyagi, N. A. Rahim, N. L. Panwar, H. Mokhlis, *Renewable Sustainable Energy Rev.* **2013**, *25*, 135 – 165.
[3] L. Zhang, X. Hu, Z. Wang, F. Sun, D. G. Dorrell, *Renewable Sustainable Energy Rev.* **2018**, *81*, 1868 – 1878.
[4] B. E. Conway, *Electrochemical Supercapacitors: Scientific Fundamentals and Technological Applications*, Kluwer Academic/Plenum, New York, **1999**.
[5] A. Burke, *J. Power Sources* **2000**, *91*, 37 – 50.
[6] J. Goodenough, H. Abruna, M. Buchanan, *Basic Research Needs for Electrical Energy Storage: Report of the Basic Energy Sciences Workshop for Electrical Energy Storage, Office of Basic Energy Sciences*, DOESC, April 2 – 4 **2007**, https://www.osti.gov/servlets/purl/935429.
[7] M. Galinski, A. Lewandowski, I. Stepniak, *Electrochim. Acta* **2006**, *51*, 5567 – 5580.
[8] M. Sha, H. Dong, F. Luo, Z. Tang, G. Zhu, G. Wu, *J. Phys. Chem. Lett.* **2015**, *6*, 3713 – 3720.
[9] S. Pohlmann, B. Lobato, T. A. Centeno, A. Balducci, *Phys. Chem. Chem. Phys.* **2013**, *15*, 17287 – 17294.
[10] A. Krause, A. Balducci, *Electrochem. Commun.* **2011**, *13*, 814 – 817.
[11] S. Pohlmann, T. Olyschläger, P. Goodrich, J. A. Vicente, J. Jacquemin, A. Balducci, *Electrochim. Acta* **2015**, *153*, 426 – 432.
[12] S. Leyva-García, D. Lozano-Castelló, E. Morallón, T. Vogl, C. Schütter, S. Passerini, A. Balducci, D. Cazorla-Amorós, *J. Power Sources* **2016**, *336*, 419 – 426.
[13] A. Borenstein, R. Attias, O. Hanna, S. Luski, R. Kaner, D. Aurbach, *ChemElectroChem* **2017**, *4*, 2660 – 2668.
[14] O. Munteshari, J. Lau, A. Krishnan, B. Dunn, L. Pilon, *J. Power Sources* **2018**, *374*, 257 – 268.
[15] O. Munteshari, J. Lau, D. S. Ashby, B. Dunn, L. Pilon, *J. Electrochem. Soc.* **2018**, *165*, A1547 – A1557.
[16] O. Munteshari, J. Lau, A. Likitchatchawankun, B-.A Mei, C. S. Choi, D. Butts, B. Dunn, L. Pilon, *Electrochim. Acta* **2019**, *307*, 512 – 524.
[17] P. W. Ruch, D. Cericola, A. Foelske, R. Kötz, A. Wokaun, *Electrochim. Acta* **2010**, *55*, 2352 – 2357.
[18] M. Hahn, A. Würsig, R. Gallay, P. Novák, R. Kötz, *Electrochem. commun.* **2005**, *7*, 925 – 930.
[19] A. L. d'Entremont, L. Pilon, *J. Power Sources* **2014**, *246*, 887 – 898.
[20] A. Likitchatchawankun, A. Kundu, O. Munteshari, T. S. Fisher, L. Pilon, *Electrochim. Acta* **2019**, *303*, 341 – 353.
[21] J. Schiffer, D. Linzen, D. Sauer, *J. Power Sources* **2006**, *160*, 765 – 772.
[22] G. Madabattula, S. Kumar, *J. Electrochem. Soc.* **2018**, *165*, A636 – A649.
[23] T. Zhang, B. Fuchs, M. Secchiaroli, M. Wohlfahrt-Mehrens, S. Dsoke, *Electrochim. Acta* **2016**, *218*, 163 – 173.
[24] Y. Dandeville, P. Guillemet, Y. Scudeller, O. Crosnier, L. Athouel, T. Brousse, *Thermochim. Acta* **2011**, *526*, 1 – 8.
[25] A. L. d'Entremont, L. Pilon, *J. Power Sources* **2016**, *335*, 172 – 188.
[26] X. Feng, X. He, M. Ouyang, L. Lu, P. Wu, C. Kulp, S. Prasser, *Appl. Energy* **2015**, *154*, 74 – 91.
[27] A. L. d'Entremont, L. Pilon, *J. Power Sources* **2015**, *273*, 196 – 209.
[28] A. Balducci, R. Dugas, P. L. Taberna, P. Simon, D. Plée, M. Mastragostino, S. Passerini, *J. Power Sources* **2007**, *165*, 922 – 927.
[29] R. S. Kühnel, A. Balducci, *J. Phys. Chem. C* **2014**, *118*, 5742 – 5748.
[30] P. M. Bayley, G. H. Lane, N. M. Rocher, B. R. Clare, A. S. Best, D. R. MacFarlane, M. Forsyth, *Phys. Chem. Chem. Phys.* **2009**, *11*, 7202 – 7208.
[31] S. T. Keaveney, K. S. S. McHale, J. W. Stranger, B. Ganbold, W. S. Price, J. B. Harper, *ChemPhysChem* **2016**, *17*, 3853 – 3862.
[32] GreenTEG, *Instruction Manual for gSKIN Heat Flux Sensors for R&D*, https://shop.greenteg.com/wp-content/uploads/gSKIN_Heat-Flux-Sensors-RD_Instructions_v2.pdf. Last accessed in Dec. **2018**.
[33] L. Pilon, H. Wang, A. L. d'Entremont, *J. Electrochem. Soc.* **2015**, *162*, A5158 – A5178.
[34] A. Burke, M. Miller, *Electrochim. Acta* **2010**, *55*, 7538 – 7548.
[35] S. Zhao, F. Wu, L. Yang, L. Gao, A. Burke, *Electrochem. Commun.* **2010**, *12*, 242 – 245.
[36] M. Stoller, R. Ruoff, *Energy Environ. Sci.* **2010**, *3*, 1294 – 1301.
[37] B.-A. Mei, O. Munteshari, J. Lau, B. Dunn, L. Pilon, *J. Phys. Chem. C* **2018**, *122*, 194 – 206.
[38] R. S. Kühnel, D. Reber, A. Remhof, R. Figi, D. Bleiner, C. Battaglia, *Chem. Commun.* **2016**, *52*, 10435 – 10438.
[39] L. Hu, D. Guo, G. Feng, H. Li, T. Zhai, *J. Phys. Chem. C* **2016**, *120*, 24675 – 24681.
[40] H.-S. Kim, J. B. Cook, S. H. Tolbert, B. Dunn, *J. Electrochem. Soc.* **2015**, *162*, A5083 – A5090.
[41] C. H. Lai, D. Ashby, M. Moz, Y. Gogotsi, L. Pilon, B. Dunn, *Langmuir* **2017**, *33*, 9407 – 9415.
[42] D. J. Bozym, B. Uralcan, D. T. Limmer, M. A. Pope, N. J. Szamreta, P. G. Debenedetti, I. A. Aksay, *J. Phys. Chem. Lett.* **2015**, *6*, 2644 – 2648.
[43] S. H. Lapidus, N. N. Rajput, X. Qu, K. W. Chapman, K. A. Persson, P. J. Chupas, *Phys. Chem. Chem. Phys.* **2014**, *16*, 21941 – 21945.
[44] T. Placke, O. Fromm, S. F. Lux, P. Bieker, S. Rothermel, H.-W. Meyer, S. Passerini, M. Winter, *J. Electrochem. Soc.* **2012**, *159*, A1755 – A1765.
[45] K. Beltrop, P. Meister, S. Klein, A. Heckmann, M. Grünebaum, H. D. Wiemhöfer, M. Winter, T. Placke, *Electrochim. Acta* **2016**, *209*, 44 – 55.
[46] S. Rothermel, P. Meister, O. Fromm, J. Huesker, H. W. Meyer, M. Winter, T. Placke, *ECS Trans.* **2014**, *58*, 15 – 25.
[47] H. C. Huang, C. W. Huang, C. T. Hsieh, H. Teng, *J. Mater. Chem. A* **2014**, *2*, 14963 – 14972.

[48] J. Newman, K. Thomas-Alyea, *Electrochemical Systems, 3rd ed.*, Wiley, Hoboken, **2003**.
[49] S. Pohlmann, R. S. Kühnel, T. A. Centeno, A. Balducci, *ChemElectroChem* **2014**, *1*, 1301 – 1311.
[50] J. Black, H. A. Andreas, *Electrochim. Acta* **2009**, *54*, 3568 – 3574.
[51] A. N. Soriano, A. M. Agapito, L. I. Lagumbay, A. R. Caparanga, M. H. Li, *J. Taiwan Inst. Chem. Eng.* **2011**, *42*, 258 – 264.

Manuscript received: November 2, 2019
Revised manuscript received: December 4, 2019
Accepted manuscript online: December 6, 2019
Version of record online: ■■ ▮▮, 0000

Potential window effect: In operando calorimetry is used to to identify the thermal signatures of the different physicochemical phenomena taking place in electrical double layer capacitors. With increasing potential window, the irreversible heat generation rate increases, exceeding Joule heating. In addition, the reversible heat generation rate increases with increasing potential window owing to the increase in the amount of ion adsorbed/desorbed at the electrode/electrolyte interface. Calorimetric measurements also identified endothermic $TFSI^-$ intercalation in the positive electrode and solvent degradation at the negative electrode above 3.5 V.

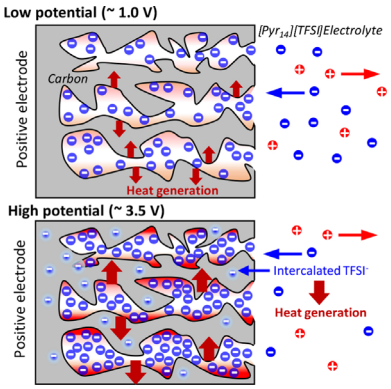

*O. Munteshari, A. Borenstein, R. H. DeBlock, J. Lau, G. Whang, Y. Zhou, A. Likitchatchawankun, R. B. Kaner, B. Dunn, L. Pilon**

■■ – ■■

In Operando Calorimetric Measurements for Activated Carbon Electrodes in Ionic Liquid Electrolytes under Large Potential Windows